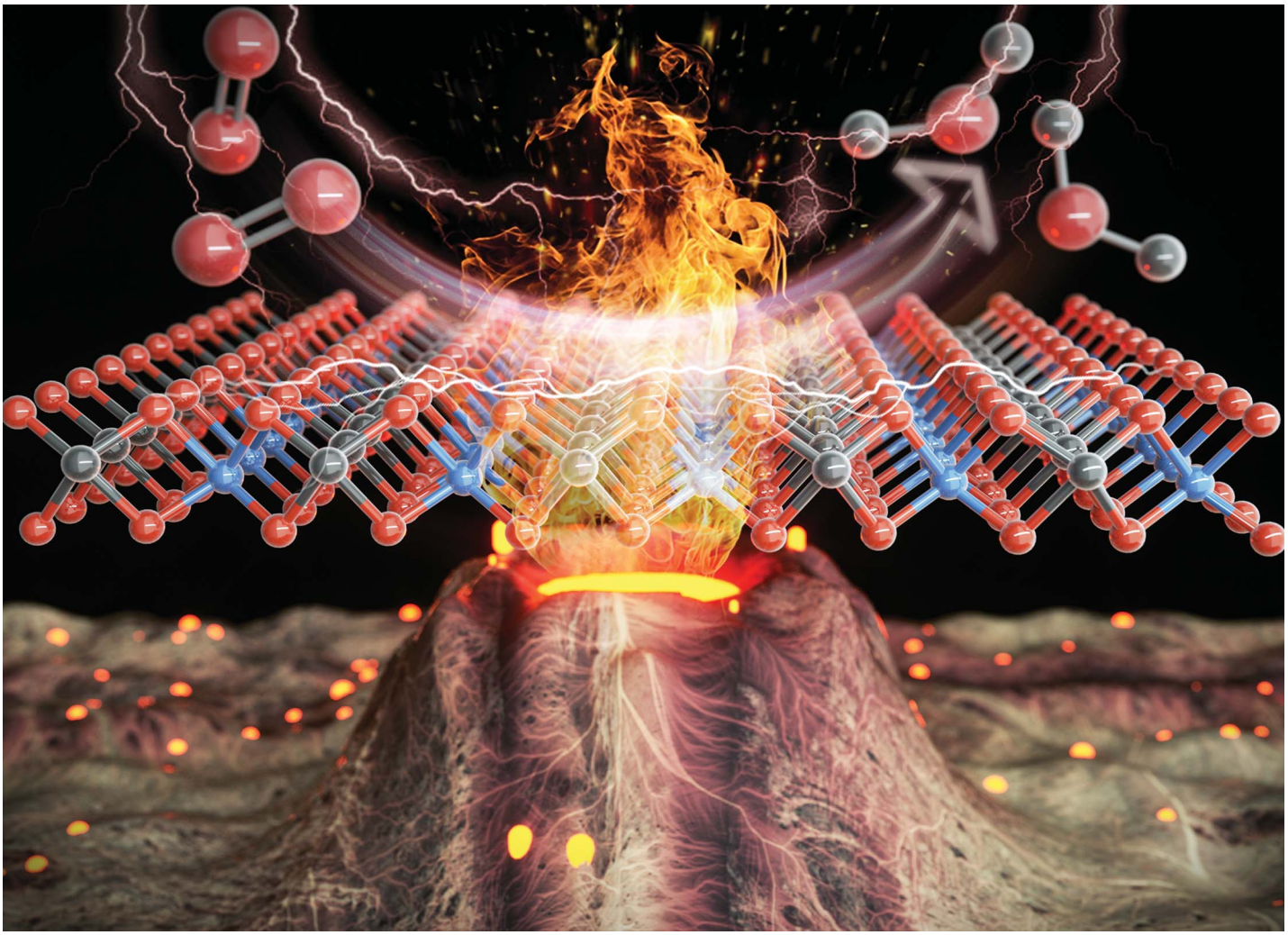

Showcasing research from Professor Yu Xie's laboratory, College of Physics, Jilin University, Changchun, China.

A theoretical roadmap for the best oxygen reduction activity in two-dimensional transition metal tellurides

The ORR catalytic performances of a series of exfoliable 2D transition-metal tellurides were investigated using density functional theory simulations. The in-depth analysis shows that the partially filled p_z state of Te atoms is responsible for the ORR activation, resulting in a physical-derived catalytic activity descriptor, the p_z-band center of Te. Based on this descriptor, the performance of the $NbRhTe_4$ monolayer was predicted to reach the top of the activity volcano with a limiting potential of 0.96 V.

As featured in:

See Yu Xie *et al.*, *Chem. Sci.*, 2022, **13**, 11048.

ROYAL SOCIETY OF CHEMISTRY

rsc.li/chemical-science

Registered charity number: 207890

Chemical Science

ROYAL SOCIETY OF CHEMISTRY

EDGE ARTICLE

View Article Online
View Journal | View Issue

Cite this: *Chem. Sci.*, 2022, **13**, 11048

All publication charges for this article have been paid for by the Royal Society of Chemistry

A theoretical roadmap for the best oxygen reduction activity in two-dimensional transition metal tellurides†

Xin Yang, [ab] Hanyu Liu, [abcd] Zexing Qu, [e] Yu Xie *[abc] and Yanming Ma [abd]

Received 1st July 2022
Accepted 23rd August 2022

DOI: 10.1039/d2sc03686j

rsc.li/chemical-science

Developing highly active and cost-effective electrocatalysts to replace Pt-based catalysts for the sluggish oxygen reduction reaction (ORR) is a major challenge in the commercialization of fuel cells. Although two-dimensional (2D) transition-metal tellurides have recently been proposed as alternative low-cost ORR catalysts, a fundamental study on the origin of the activity is required to further optimize their composition and performance. Herein, we investigated the electronic properties and ORR catalytic performances of a series of exfoliable 2D transition-metal tellurides to uncover the underlying mechanisms by means of density functional theory simulations. Our in-depth analysis shows that the activation of the ORR mainly depends on the partially filled p_z state of active Te atoms, which can simultaneously accept and donate electrons behaving similarly to both the occupied and unoccupied d orbitals of Pt atoms. This results in a linear relationship between the p_z-band center and the adsorption free energies of O_2 and intermediates, indicating that the p_z-band center might be used as an effective descriptor to probe the performance of telluride catalysts. On this basis, we predicted several 2D transition-metal tellurides with promising catalytic performance and reduced precious-metal contents, where $NbRhTe_4$ reaches the top of the activity volcano with a limiting potential of 0.96 V. This study provides theoretical guidance to design high-performing 2D telluride ORR catalysts, and its principle might be applicable to other electrochemical reactions in 2D chalcogenides.

Introduction

Proton exchange membrane fuel cells (PEMFCs) are recognized as one of the most effective technologies for growing clean and sustainable energy demands, as they can directly convert chemical energy into electricity.[1–3] Generally, the overall performance of PEMFCs depends largely on the kinetics of the cathodic oxygen reduction reaction (ORR), as it is much slower than the anodic hydrogen oxidation reaction (HOR), and other reactions including the hydrogen evolution reaction (HER) and oxygen evolution reaction (OER).[4] The key to overcoming this bottleneck is finding highly efficient catalysts to boost the sluggish ORR kinetics, which are currently dominated by Pt-based catalysts (*e.g.*, Pt nano-frameworks and Pt alloys) owing to their high activity and good stability.[5–7] However, the high cost of Pt-based catalysts significantly hampers large-scale applications of PEMFCs.[8,9] Thus, there is an urgent need to design highly efficient ORR catalysts with a reduced Pt (precious metal) content for the sustainable development of fuel cells.

Emerging two-dimensional (2D) materials have shown great potential as efficient catalysts owing to their high specific surface area and minimum migration distance for carriers.[10–14] Among them, doped transition metal dichalcogenides (TMDs) and metal(M)–N–C single-atom catalysts (SACs), produced by embedding atomically dispersed metal species into graphene, were found to exhibit good ORR catalytic activity.[15–19] Unfortunately, the advantages of 2D morphology for most of these materials are not well utilized, because their pristine basal planes are catalytically inactive. To fully leverage the potential of 2D materials for the catalytic ORR, it is essential to seek 2D catalysts with high basal plane activity, where there has recently been increasing attention focused on metallic transition metal telluride monolayers.[20–28] For instance, layered $PtTe_2$ was demonstrated to show ORR activity on par with the commercial Pt/C catalyst.[21] Monolayer PtTe was predicted to have a limiting potential of 0.86 V,[22] which outperforms Pt (111) electrodes (0.78 V). The precious metal free NiTe and $TaTe_2$ monolayers

[a]*State Key Laboratory of Superhard Materials, College of Physics, Jilin University, Changchun 130012, China. E-mail: xieyu@jlu.edu.cn*

[b]*International Center of Computational Method and Software, College of Physics, Jilin University, Changchun 130012, China*

[c]*Key Laboratory of Physics and Technology for Advanced Batteries (Ministry of Education), College of Physics, Jilin University, Changchun 130012, China*

[d]*International Center of Future Science, Jilin University, Changchun 130012, China*

[e]*Institute of Theoretical Chemistry, College of Chemistry, Jilin University, Changchun, 130023, China*

† Electronic supplementary information (ESI) available: Details of computational methods, structures, electronic properties, adsorption energies, energy barriers of O_2 dissociation, free energy diagrams and linear relationships. See https://doi.org/10.1039/d2sc03686j

were soon after demonstrated with similar catalytic performance compared to Pt electrodes.[23] The activity of 2D Ni_2SbTe_2 was also recently examined,[27] where the endothermic O_2 adsorption might prohibit the ORR process on the basal plane. Although 2D transition metal tellurides indeed exhibit excellent catalytic activity towards the ORR, PtTe, with currently the best overall performance, still contains a large amount of the precious metal (50% formula weight) hindering its practical applications. Rational design of transition metal tellurides is desired to achieve better performance in both cost and catalytic activity. This remains untouched, primarily due to the lack of knowledge of the ORR activity origin of tellurides. In particular, unlike Pt-based catalysts, the electronic characteristics of Te atoms vary in different tellurides, as the electronegativity difference between Te and the transition metal is different. Thus, elucidating the catalytic activity origin of the Te atom is fundamental in the design of high-performing 2D telluride ORR catalysts that may extend to other chalcogenides.

In this study, we theoretically explore the ORR catalytic performance of a series of 2D stable nanosheets, $NbTe_2$, WTe_2, $MoTe_2$, and $M_xX_yTe_z$ nanosheets (M = Nb and Ta and X = transition metals), which can readily be exfoliated from their bulk phases.[29–37] By combining the electronic density of states and molecular orbital analysis, we found that the partially filled p_z state of Te atoms can simultaneously accept electrons from the orbital and donate electrons to the π^* orbital of the O_2 molecule, endowing telluride nanosheets with activities for O_2 fixation and protonation. The adsorption energies of O_2, O, and OH are thus linearly related to the p_z-band center of Te atoms, where the closer the band center to the Fermi level, the stronger the binding of the adsorbates. The constructed ORR activity volcano plot allows the p_z-band center derivation between −2.5 and −1.8 eV for telluride monolayers with potentially high activity. Following this guidance, several telluride monolayers, such as $MXTe_4$ and $Ta_4Pd_3Te_{16}$, were identified with limiting potentials of 0.73–0.96 V in the four-electron ($4e^-$) pathway and precious-metal contents of less than 24%, implying that they are potentially highly performing ORR catalysts.

Results and discussion

Geometric and electronic properties

We first selected nine telluride monolayers with various stoichiometries and compositions in conjunction with previously studied 2D telluride catalysts to probe the nature and origin of the electrocatalytic ORR activity of telluride nanosheets. The selected nine tellurides are $NbTe_2$, WTe_2, $NbNiTe_2$, $TaCo_2Te_2$, $TaNi_2Te_3$, $NbIrTe_4$, $NbPdTe_5$, $Ta_2Pd_3Te_5$, and $Ta_3Pd_3Te_{14}$ (Fig. 1). Because all of these 2D tellurides have experimentally synthesized bulk counterparts,[29–37] the cleavage energies (E_{cl}) were evaluated to assess the experimental exfoliation feasibility by using a five-layer slab. As presented in Fig. S1,† the E_{cl} of $NbTe_2$, WTe_2, $TaNi_2Te_3$, $NbIrTe_4$, and $NbPdTe_5$ are comparable to that of exfoliated 2D MoS_2 (0.42 J m^{-2}),[38] which can be classified as easily exfoliated according to the report of Mounet and coworkers.[39] Other telluride nanosheets have slightly higher E_{cl} and can be regarded as potentially exfoliated. Therefore, isolation of these 2D tellurides from their parent phases *via* exfoliation is experimentally feasible. Structurally, each nanosheet comprises transition metal atomic layers sandwiched between two Te atomic layers, where $NbTe_2$, WTe_2, $NbIrTe_4$, $NbPdTe_5$, and $Ta_3Pd_3Te_{14}$ comprise one metal layer, while others comprise two or three metal layers. Specifically, $NbTe_2$, WTe_2, and $NbIrTe_4$ are composed of MTe_6 (XTe_6) octahedra. Similarly, $TaNi_2Te_3$ consists of XTe_4 tetrahedra and MTe_6 octahedra, which are also contained in $Ta_2Pd_3Te_5$, where one of the octahedral apexes is X (MTe_5X octahedra). $NbPdTe_5$ and $Ta_3Pd_3Te_{14}$ are formed of MTe_8 decahedra and MTe_6 (XTe_6) octahedra. The rest of the two tellurides, $NbNiTe_2$ and $TaCo_2Te_2$, do not possess the above polyhedra. The dynamic stability of the monolayers was confirmed from their computed phonon frequencies, as reported in Materials Cloud two-dimensional crystals databases[39] and database C2DB[40] of 2D materials. The calculated band structures and density of states (DOS) of the above nanosheets reveal that $NbIrTe_4$ is semi-metallic with a zero bandgap that exhibits metallic behaviors,[41] and the other nanosheets are well-defined metals (Fig. S2†). Moreover, we also

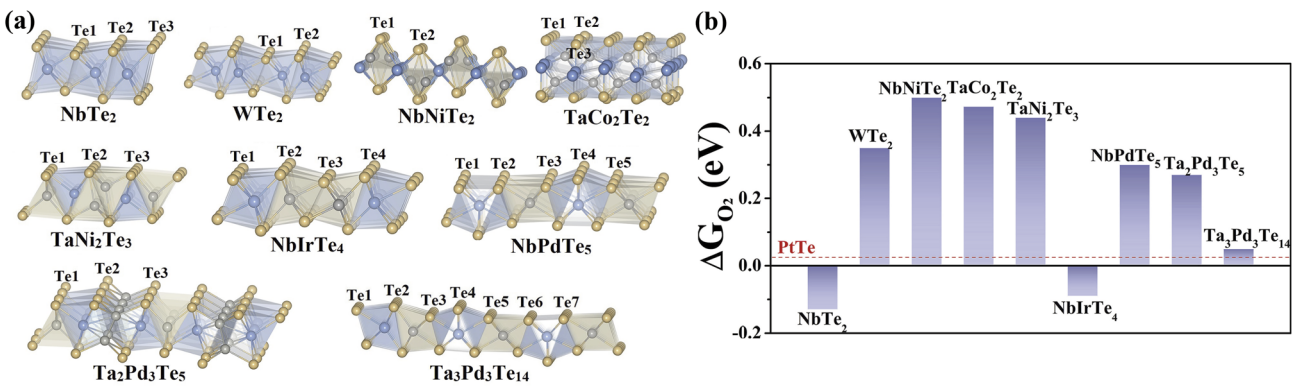

Fig. 1 (a) Side views of optimized structures of monolayer $NbTe_2$, WTe_2, $NbNiTe_2$, $TaCo_2Te_2$, $TaNi_2Te_3$, $NbIrTe_4$, $NbPdTe_5$, $Ta_2Pd_3Te_5$, and $Ta_3Pd_3Te_{14}$. The blue, grey and yellow balls represent M, X, and Te atoms, respectively. (b) The O_2 adsorption energy of monolayer tellurides.

examined the charge distribution of these tellurides through the Bader charge analysis. As shown in Table S1,† most Te atoms are negatively charged due to the charge transfer from inner transition metal atoms to outer Te atoms. Only Te_3 atoms in $NbIrTe_4$ are positively charged with around 0.25 *e* transferred from Te to Ir.

Origin of O_2 activation

After determining the stability and electronic properties of these nanosheets, we proceeded to explore the adsorption of the O_2 molecule, which is the prerequisite for an efficient ORR process. The most favorable O_2 adsorption configurations and calculated adsorption energies (ΔG_{O_2}) are shown and summarized in Fig. 1b and S3, and Table S2–3.† The ΔG_{O_2} of $NbTe_2$ and $NbIrTe_4$ monolayers is −0.13 and −0.09 eV, respectively, suggesting that O_2 can be chemisorbed. The moderate ΔG_{O_2} of 0.05 eV indicates that O_2 might be physisorbed on the $Ta_3Pd_3Te_{14}$ monolayer that is similar to the PtTe monolayer. Other telluride monolayers possess ΔG_{O_2} larger than 0.20 eV, where the endothermic nature suggests that O_2 molecules are hardly adsorbed on these telluride monolayers to trigger the ORR process. Moreover, the O–O bond length is significantly stretched from 1.23 Å in the gas phase to 1.38 and 1.39 Å when O_2 is adsorbed on $NbTe_2$ and $NbIrTe_4$, respectively. The weakening of O–O bonds is expected to facilitate the subsequent ORR steps. From the nudged-elastic-band (NEB) calculations, the energy barriers of O_2 dissociation into two adsorbed O* are around 0.42 and 0.54 eV for $NbTe_2$ and $NbIrTe_4$, respectively (Fig. S4†), which are comparable to the O_2 dissociation barrier on Pt (111) (0.38–0.50 eV),[42,43] indicating that O_2 has been effectively activated.

Since O_2 activation plays a crucial role in the ORR process, uncovering the origin of O_2 adsorption is beneficial for designing efficient ORR catalysts. Previously, an electron activation mechanism was proposed for the positively charged Te in the PtTe monolayer.[22] According to this mechanism, the Te–O bond strength depends on the number of electrons the Te atom gains/loses (N_e), where the smaller N_e leads to stronger binding of O_2. Thus, we examined the correlation between N_e and ΔG_{O_2} of the studied telluride monolayers (Fig. S5†). Unlike the observed linear relationship between N_e and the binding energy of adsorbates in other systems, we found that ΔG_{O_2} does not depend on N_e. Either the positively or negatively charged Te atom can activate the O_2 molecule. Moreover, for most telluride monolayers, a larger N_e causes a stronger adsorption of O_2 that is opposite to the proposed mechanism. Therefore, O_2 adsorption cannot be simply described by the electron activation mechanism.

To gain a better understanding of the underlying O_2 adsorption mechanism, we further analyzed the orbital configuration of Te atoms in comparison with Pt-based catalysts. For the Pt atom (Fig. 2a), the coexistence of unoccupied and occupied d orbitals can facilitate O_2 adsorption and activation through a two-way charge transfer, where the unoccupied e_g orbital accepts lone-pair electrons from O_2, and the occupied t_{2g} orbital donates electrons back to O_2 antibonding orbitals.[44,45] This donation and back-donation concept is standard in molecular chemistry (Blyholder model) and has been successfully employed to describe the interaction between small molecules (*e.g.*, N_2, C_2H_4, and CO) and transition metal and boron-based catalysts.[46–53] Interestingly, the Te atom possesses an orbital configuration analogous to that of Pt and B atoms in transition metal stuffed boron nitride nanotubes. As illustrated in Fig. 2b, the valence electronic configuration of the Te atom is $5s^25p^4$ regardless of the charge transfer between Te and transition metal atoms, resulting in one fully occupied p orbital and two partially filled p orbitals. Therefore, the Te atom is eligible to drive a similar "donation and back-donation" process to adsorb the O_2 molecule, as shown in Fig. 2b.

To verify our inference, the charge density difference between O_2* and telluride monolayers was calculated to reveal the underlying charge transfer. As shown in Fig. S6–9,† O_2* exhibits a clear picture of the two-way charge transfer exhibiting charge accumulation (yellow) and depletion (blue). Interestingly, Te atoms seem to deviate from this mechanism as electrons barely accumulate around them.

To decipher this phenomenon, we then evaluated the O–O and O_2–Te interactions by a combined electronic structure and projected crystal orbital Hamilton populations (pCOHP) analysis, taking the $NbIrTe_4$ monolayer as an example. The quantity of −(pCOHP) was used to directly correspond the positive and negative values with bonding and antibonding states, respectively. The molecular orbital (MO) diagram, projected density of states (pDOS), and pCOHP of the free O_2 molecule were examined first, as presented in Fig. S10.† By analyzing the pDOS and pCOHP, it is clear that the fully occupied 5σ and 1π orbitals contribute to the bonding of the O_2 molecule, while the partially filled $2\pi^*$ orbital is antibonding.

After O_2 adsorption on the $NbIrTe_4$ monolayer, the sharp localized MOs of O_2 in a vacuum hybridize with surface Te p states that broaden into rather delocalized states and shift down to lower energy (Fig. 2c). The new hybrid states are marked as "tildes" of the original orbitals to indicate the difference (Fig. S11†). The $5\tilde{\sigma}$ band showed up in a narrow energy range at around −7.05 eV relative to the Fermi level, and the electron density of the $5\tilde{\sigma}$ band is reduced compared to the 5σ orbital of free O_2. This agrees with the Blyholder picture of σ forward donation, as reflected by the flow of 0.23 electrons from O_2 to Te atoms, resulting in the formation of a novel Te DOS peak, mainly composed of the p_z state of the Te1 atom in the same energy range and σ-type Te–O bonds (Fig. S6–9).† The degenerated 1π MO split into two narrow 1π bands at around −6.4 and −5.5 eV, respectively, and broad bands $\tilde{P}_{1\pi}$ and $\tilde{P}_{2\pi^*}$ between −5.3 and −1.1 eV upon hybridization with Te states and $2\pi^*$ MO. Importantly, the unoccupied $2\pi^*$ MO of free O_2 became partially populated and transformed into $2\tilde{\pi}^*$ bands in the energy range between −1.0 and 2.3 eV, where 0.5 electrons were back-donated from the Te atom to the $2\pi^*$ orbital of O_2 (Fig. S6†). The net charge transfer from Te to O_2 agrees with the Bader charge analysis, as O has a higher electronegativity, implying that the back-donation is a more dominant Te–O interaction. Interestingly, p_z of the Te_1 atom was also the main contribution for the back-donation. Therefore, Te atoms could

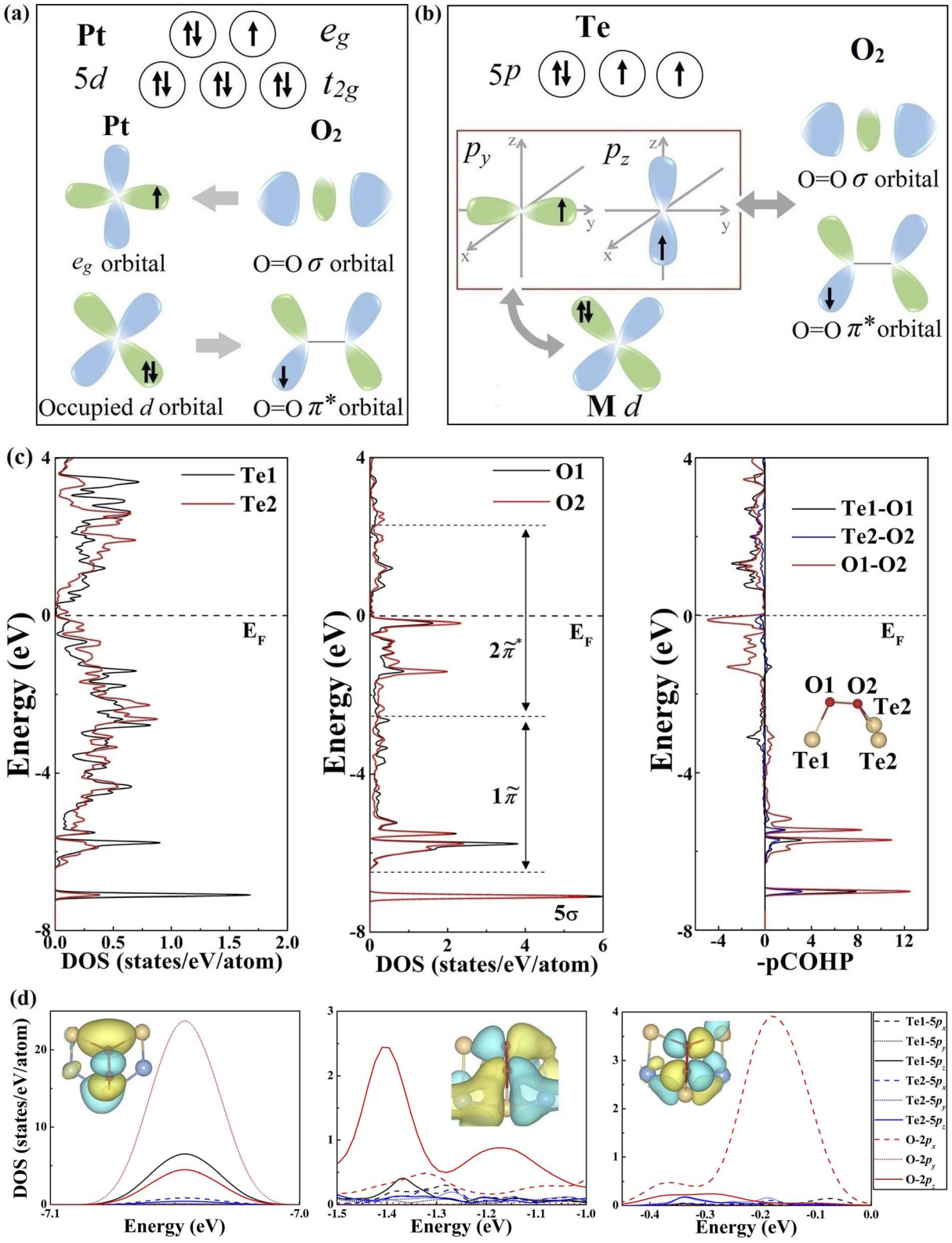

Fig. 2 (a) Simplified schematic of O_2 bonding to Pt. (b) Mechanism of activation of monolayer $NbIrTe_4$ for O_2 adsorption (c) DOS and pCOHP curves of O_2-adsorbed tellurides. The orbitals of O_2 in O_2-adsorbed tellurides are marked here. (d) pDOS and the corresponding molecular orbital of the O_2-adsorbed $NbIrTe_4$ monolayer.

accept and donate electrons from and to O_2 molecules simultaneously, while the p_z orbital of the Te_1 atom contributes the most. The electron depletion of Te can thus be understood, as the two-way charge transfer mainly takes place in the same orbital, and the net charge transfer between Te and O_2 is negative. Other studied telluride monolayers, such as PtTe, $NbTe_2$, and $Ta_3Pd_3Te_{14}$, also present the same phenomenon (Fig. S7–9).† Therefore, the origin of O_2 activation on 2D tellurides is a unique "donation and back-donation" mechanism that stretches and weakens the O–O bond.

ORR catalytic performance

We assessed the catalytic performance of telluride monolayers for the reduction of O_2 to H_2O. The typical association and dissociation mechanisms (Fig. 3), including all possible intermediate reactants (Fig. S12 and 13)† were widely investigated for $NbTe_2$, $NbIrTe_4$, and $Ta_3Pd_3Te_{14}$ monolayers. For other telluride monolayers, we only calculated the adsorption energies of O and OH for comparison. As illustrated in Fig. 3, the $NbTe_2$ monolayer shows similar catalytic behaviors to the $TaTe_2$ monolayer,[23] where the association pathway has a higher limiting potential (U_L) of 0.80 V (OH* reduction to H_2O) than the dissociation pathway of 0.63 V (Fig. S12†), suggesting that the association mechanism exhibits higher efficiency. Alternatively, the dissociation mechanism is more efficient in $NbIrTe_4$ and $Ta_3Pd_3Te_{14}$ monolayers, as their U_L of 0.88 and 0.80 V (O* reduction to OH*) are higher than the association ones of 0.65 and 0.45 V (O_2 to OOH*), respectively (Fig. 3 and S13†). In addition to the 4e electrochemical processes, we also examined the 2e reduction pathways for the dominant reduction mechanism. The free energy diagrams show that the U_L of the 2e association pathway is 0.6 V for the $NbTe_2$ monolayer, which is lower than that of the 4e association pathway. The H_2O_2 formation is endothermic for the dissociation pathway of $NbIrTe_4$ and $Ta_3Pd_3Te_{14}$ monolayers, indicating that it is difficult to occur during the ORR process. These results suggest that $NbTe_2$, $NbIrTe_4$, and $Ta_3Pd_3Te_{14}$ monolayers are rather good ORR catalysts with high 4e pathway selectivity. Considering that monolayers are generally more difficult to obtain than multilayers, we also explored the electrocatalytic performance of bilayer and trilayer $NbIrTe_4$ (Fig. S14–16†). The electrocatalytic

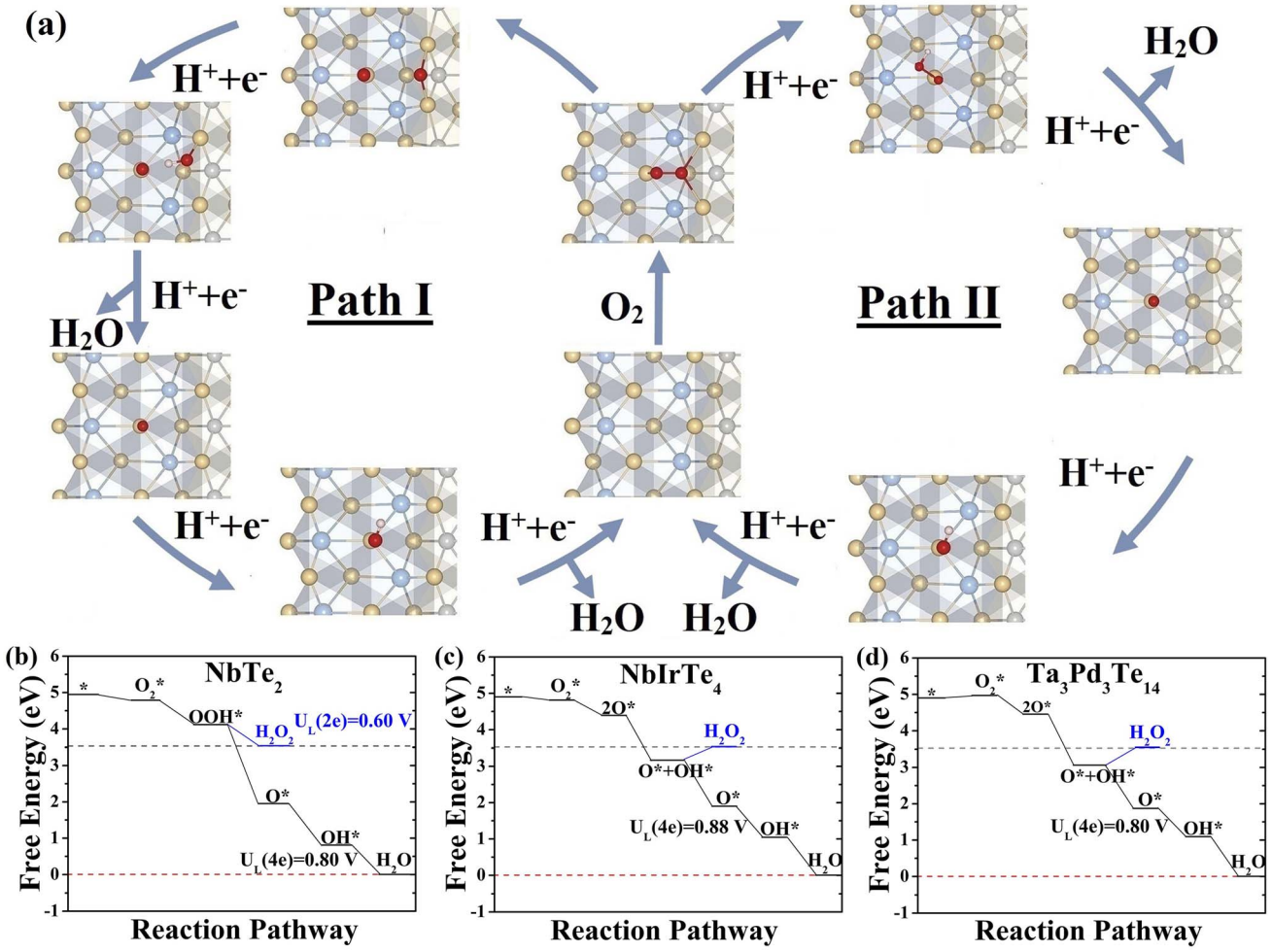

Fig. 3 (a) Scheme of the possible two ORR reaction pathways of monolayer $NbIrTe_4$. Calculated free energy diagrams for the ORR pathway on monolayer (b) $NbTe_2$ in an association pathway and (c) $NbIrTe_4$ and (d)$Ta_3Pd_3Te_{14}$ in a dissociation pathway.

performance of bilayer and trilayer $NbIrTe_4$ is similar to that of the monolayer with limiting potentials of 0.89 and 0.81 V.

A previously established theory for transition metal-based catalysts suggested that the adsorption energies of O-containing intermediates, governing the catalytic performance, are linearly correlated.[54–60] Thus, the catalytic activity can be described by the adsorption energies of a single intermediate reactant. Similar to transition metal-based catalysts, linear scaling relationships between ΔG_{OH^*} and other reactants were also identified in telluride monolayers (Fig. 4a and S17†). For example, ΔG_{OH^*} and ΔG_{OOH^*} are related to each other by a constant of approximately 3.3 eV that is close to 3.2 eV, observed in transition metal-based catalysts (Fig. S17b†). Given the excellent linear relationship, we plotted U_L as a function of ΔG_{OH^*} for telluride monolayers, where the transition metal-based catalysts were also included for comparison (Fig. 4b).[22,23,27,61,62] This leads to the observation of a universal volcano relationship that follows the century-old Sabatier principle, where an ideal catalyst must bind the intermediate reactants with an intermediate strength: not too weak to activate the reactants, and not too strong to desorb the products. The estimated highest limiting potential is approximately 0.94 V, which demonstrates that the dissociation pathway can elevate the limiting potential close to 0.1 V compared with the previously suggested U_L of 0.86 V for an ideal ORR catalyst. For an efficient catalyst with a limiting potential higher than that of Pt (111), one should search for tellurides with a ΔG_{OH^*} between 0.8 and 1.2 eV.

Activity descriptor

Since the simulated limiting potential of 2D tellurides relates well to the binding energy of intermediate adsorbates, similarly to that of transition metal-based catalysts, we proceed to seek a simple descriptor that can correlate the adsorption energy with the intrinsic properties of tellurides like the *d*-band center model for transition metals.[50,65–70] As we already know that the partially filled p_z orbital is responsible for the Te–O interactions upon O_2 adsorption, we introduced a descriptor ε_{pz} defined as the centroid of the projected density of states of the p_z orbital relative to the Fermi level analogous to the d-band center.[71–75] As presented in Fig. 4c and d, ε_{pz} of the active Te atoms shows a reasonable linear relationship to the adsorption energies of O_2 and intermediate oxygen-containing adsorbates. The linear relationships between ΔG_{O_2} and other possible descriptors, such as the p-band center ε_p, are also calculated as shown in Fig. S18,† all of which are inferior to that of ε_{pz}. Similar to the *d*-band center model, the closer the ε_{pz} to the Fermi level, the stronger the binding strength of the adsorbates on telluride monolayers.[63] This can be understood through the bond order, which is half of the difference between the electron number of the bonding orbital and the antibonding orbital according to molecular orbital theory. A high bond order corresponds to strong binding and *vice versa*. When O-containing groups are adsorbed on telluride monolayers, the O 2p orbitals hybridize with the Te $5p_z$ orbital forming a fully filled bonding state and partially filled antibonding state. A high ε_{pz} results in a low

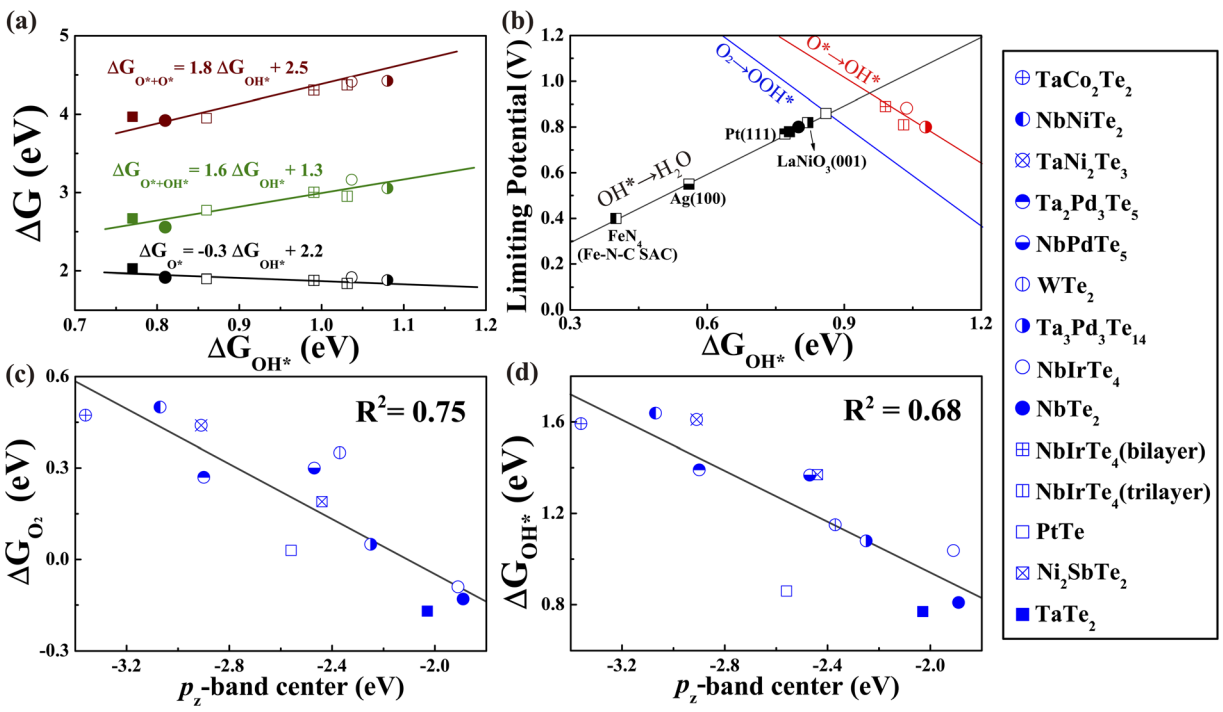

Fig. 4 (a) The variation of adsorption energy of intermediate adsorbates in the ORR dissociation pathway as a function of ΔG_{OH}* (b) Volcano plot of the ORR limiting potentials for studied tellurides and other known catalysts.[15,22,23,63,64] The blue line (O_2 to OOH*) was taken from previous work.[64] Other details are shown in Fig. S17.† (c) The O_2 adsorption energy and (d) OH adsorption energy *versus* the p_z-band center of active Te sites for initially studied monolayer tellurides.

filling of the antibonding state and hence a large bond order that could lead to enhanced Te–O binding strength. On the contrary, a low bond order corresponding to low ε_{pz} and high filling of the antibonding state weakens the telluride-adsorbate interaction, destabilizing the Te–O bond. In this sense, the p_z-band center, ε_{pz}, can serve as a simple catalytic activity descriptor for telluride monolayers. An efficient 2D telluride catalyst with a ΔG_{OH^*} between 0.8 and 1.2 eV and the ability for O_2 chemisorption are predicted to possess a ε_{pz} between −2.5 and −1.8 eV. Thus, we obtained the screening criterion.

Rational screening of efficient ORR catalysts

With the established activity descriptor, we moved on to search for potential 2D telluride catalysts that may possess a better catalytic performance. We further evaluated the electronic properties of T_d-$MoTe_2$, $TaNiTe_2$, $NbRhTe_4$, $TaRhTe_4$, $TaIrTe_4$, $Ta_2Ni_3Te_5$, and $Ta_4Pd_3Te_{16}$ monolayers. Except for $NbRhTe_4$, the bulk phases of these monolayers have also been experimentally synthesized.[29,76–78] The thermodynamic stability of bulk $NbRhTe_4$ was confirmed by constructing the Nb–Rh–Te ternary phase diagram as shown in Fig. S19(a),† which is in line with previous theoretical studies.[79,80] As shown in Fig. S19(b),† the isolation of these 2D tellurides from their bulk phases *via* exfoliation is experimentally feasible. Among them, $NbRhTe_4$, $TaRhTe_4$, $TaIrTe_4$, and $Ta_4Pd_3Te_{16}$ have ε_{pz} values between −2.5 and −1.8 eV that meet the criteria for efficient ORR catalysts. Thus, as previously, we focused on the catalytic activity of these four tellurides for both dissociation and association pathways and calculated the adsorption free energies of the rest of the tellurides for comparison and construction of the correlation. The calculated ΔG_{O_2} shows that O_2 molecules can be chemisorbed on $NbRhTe_4$, $TaRhTe_4$, $TaIrTe_4$, and $Ta_4Pd_3Te_{16}$ to trigger the ORR process as expected. The free energy diagrams (Fig. S20–22)† show that the dissociative pathway generally exhibits higher limiting potential than the associative pathway. The rate limiting step is OH* to H_2O, O* to OH*, O* to OH*, and O + OH* to O* for $NbRhTe_4$, $TaRhTe_4$, $TaIrTe_4$, and $Ta_4Pd_3Te_{16}$, respectively. The corresponding limiting potentials are all above 0.78 eV, which are comparable to that of Pt (111) and the PtTe monolayer. Encouragingly, these $MXTe_4$ and $Ta_4Pd_3Te_{16}$ tellurides contain small amounts of precious metals of 17% and 13% formula weight. In particular, the $NbRhTe_4$ monolayer has a limiting potential as high as 0.96 V, that is close to the predicted U_L of 0.94 V for an ideal catalyst, indicating that the $NbRhTe_4$ monolayer could reach the top of the 4e ORR activity volcano (Fig. 5b). Herein, we also explored the electrocatalytic performance of bilayer and trilayer $NbRhTe_4$ (Fig. S23†). The limiting potential of bilayer and trilayer $NbRhTe_4$ is similar to that of the monolayer with 0.95 and 0.85 V.

Notably, the newly identified promising $MXTe_4$ type telluride catalysts can be viewed as X substituted MTe_2 (50% substitution). Thus, by varying the substitution ratio, we may obtain potential telluride catalysts with an even lower precious-metal content, while maintaining high activity, as they should

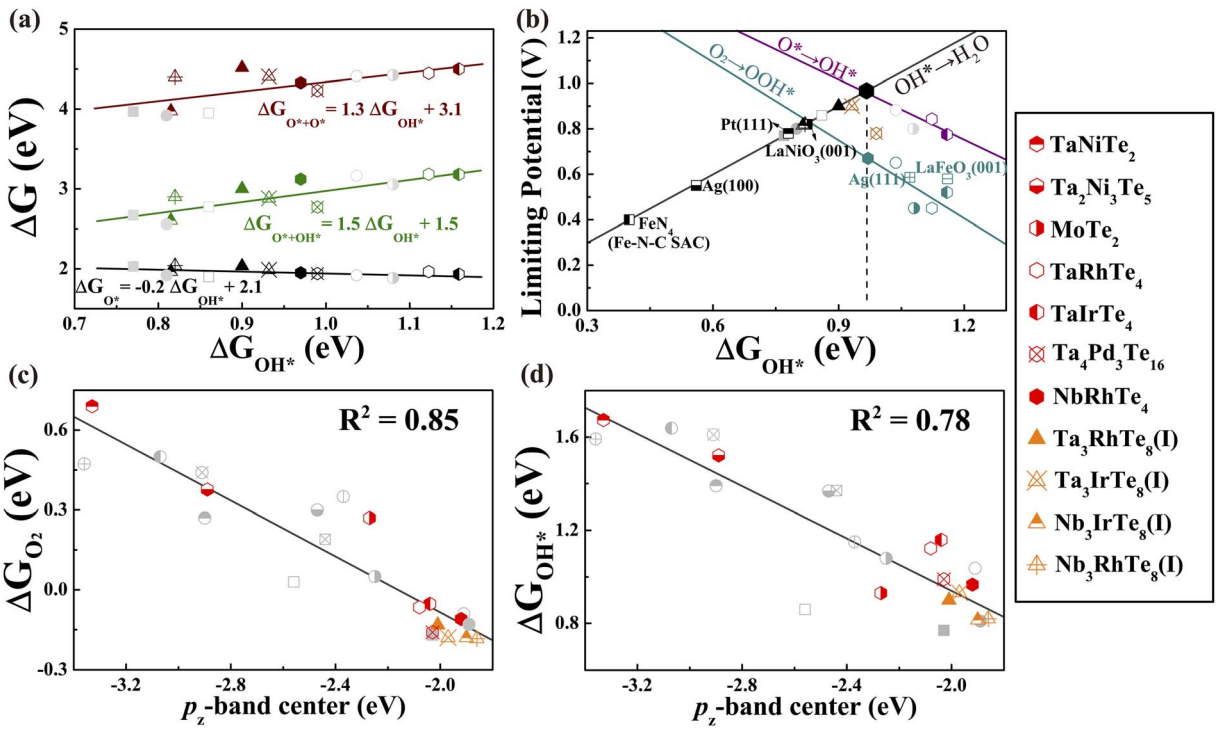

Fig. 5 (a) The variation of adsorption energy of intermediate adsorbates in the ORR dissociation pathway as a function of ΔG_{OH}*. (b) Volcano plot of the ORR limiting potentials for all studied monolayer tellurides and other known catalysts. (c) The O_2 adsorption energy and (d) OH adsorption energy *versus* the p_z-band center of active Te sites for all studied monolayer tellurides. The grey circle and square points represent initially studied tellurides and known catalysts in other studies[15,22,23,63,64] shown in Fig. 4. The star and triangle points represent newly studied tellurides and M-doped variants, respectively.

possess ε_{pz} close to that of $MXTe_4$ or MTe_2 monolayers. Hence, we designed two hypothetical M_3XTe_8 (25% substitution) structures, phase I and II that possess similar energies, as a tentative attempt (Fig. S24a and b†). The calculated formation energy of the bulk phases of these hypothetical monolayers was between 20 and 25 meV/atom, suggesting that the hypothetical M_3XTe_8 phases are metastable and might be realized in the experiments (Fig. S24†). Similarly, we considered both dissociation and association pathways. Fig. S25 and 26† presented the detailed ORR process and the calculated free energy diagrams of phase I Nb_3RhTe_8, Ta_3RhTe_8, Ta_3IrTe_8, and phase II Nb_3IrTe_8, which showed better ORR performance in these two phases (the details of another phase are summarized in Table S4 and S5†). As shown in the free energy diagrams, the limiting-potential of phase I of Nb_3RhTe_8 and Ta_3RhTe_8, and phase II of Nb_3IrTe_8 is predicted to be 0.82, 0.90, and 0.81 V, respectively, with the limiting step of $OH^* \rightarrow H_2O$. Differently, the limiting step of phase I of Ta_3IrTe_8 is predicted to be $O + OH^* \rightarrow O^*$, with a ΔG of −0.90 eV. These hypothetical substituted monolayers show superior ORR activity with a decreased precious-metal content (8%).

Finally, we re-examined the correlation between the adsorption energies of oxygen-containing groups and ε_{pz} by including all studied telluride monolayers. A better linear relationship between $\Delta G_{adsorbates}$ and ε_{pz} was also observed (Fig. 5c, d and S27†), indicating that all these 2D telluride catalysts should have a similar underlying mechanism, and the p_z orbital is primarily responsible, so that ε_{pz} could be used to describe the interaction between reactants and substrates. Therefore, once the optimal ε_{pz} is established, one can rationally design highly active 2D telluride-based ORR catalysts through this simple activity descriptor. Notably, as we only considered transition metal tellurides in the current study, a large discrepancy may occur for the catalytic activity prediction of tellurides containing main-group elements or with different activation mechanisms, where the descriptor should be corrected accordingly.

Conclusions

In summary, systematical density functional theory calculations were employed to investigate the nature and origin of ORR activities of a series of experimentally synthesizable 2D transition-metal telluride catalysts. Our results suggested that the partially occupied p_z state of Te atoms can effectively drive the "donation-back-donation" process through a two-way charge transfer, playing an important role in the activation of O_2. The subsequent O_2 reduction processes proceed through the four-electron pathway, where most of the tellurides take the dissociative pathway. The binding strength of O_2 and intermediates is linearly dependent on the p_z-band center, implying that the latter can serve as an indicator to probe the catalytic activity of tellurides. By adopting this concept to justify the volcano plot between the limiting potential and OH adsorption free energy, we predicted that $MXTe_4$, $Ta_3Pd_3Te_{14}$, and $Ta_4Pd_3Te_{16}$ are potential ORR catalysts, where $NbRhTe_4$ shows the highest limiting potential of 0.96 V among studied transition metal telluride catalysts, reaching the top of the activity volcano with a precious-metal content of only 17%. The hypothetical substitution of $MXTe_4$ leads to Ta_3IrTe_8 with a limiting potential of 0.90 V and a precious-metal content of 8%. Our study demonstrates that transition metal telluride nanosheets are highly compelling ORR electrocatalysts and proves the generality of the physically derived descriptor for screening active tellurides. We further expect the presented strategy to be extended to other electrocatalysis processes to identify descriptors to rationally and efficiently design highly active catalysts among 2D chalcogenides.

Methods

Density functional theory computations were performed by using the Vienna *Ab initio* simulation package (VASP) within the projected augmented wave method.[81,82] The Perdew–Burke–Ernzerhof (PBE) functional in the generalized gradient approximation (GGA) was used to describe the exchange-correlation potential.[83] A plane-wave energy cut-off of 500 eV was used, and all atoms were fully relaxed using the conjugate gradient algorithm with a criterion of convergence of 10^{-5} eV and 0.03 eV per atom.[84] For multilayer systems, the DFT-D3 empirical correction was used to describe van der Waals (vdW) interactions, which has been proven reliable for describing long-range vdW interactions.[85] The phonon spectra of 2D tellurides were computed using the finite displacement method, as implemented in the Phonopy code.[86] Bader's quantum theory of atoms in molecules (QTAIM) analysis was employed for the charge transfer calculations.[87] The bonding was further analyzed by calculating the projected crystal orbital Hamilton populations (pCOHPs) using the LOBSTER package.[88–90] The energy barriers were calculated using the climbing image nudged-elastic-band (CI-NEB) methods implemented in the VASP.[91] The ORR processes were calculated on the basis of the computational hydrogen electrode (CHE) model.[92]

Data availability

The data supporting the findings of this study are available in the manuscript and ESI† and from the corresponding author upon reasonable request.

Author contributions

Yu Xie conceived the presented idea. Xin Yang, Zexing Qu, and Yu Xie performed the first-principles calculations. Xin Yang, Hanyu Liu, Yu Xie and Yanming Ma wrote the manuscript. All authors discussed the results and assisted during manuscript preparation.

Conflicts of interest

There are no conflicts to declare.

Acknowledgements

This work was supported by the National Natural Science Foundation of China (Grant no. 12022408), the Interdisciplinary Integration and Innovation Project of JLU, Fundamental Research Funds for the Central Universities and the Program for JLU Science and Technology Innovative Research Team (JLUSTIRT). This paper is dedicated to the 70th anniversary of College of Physics of Jilin University. Part of the calculations were performed at the High Performance Computing Center of Jilin University.

Notes and references

1 B. C. H. Steele and A. Heinzel, *Nature*, 2001, **414**(6861), 345–352.
2 M. K. Debe, *Nature*, 2012, **486**(7401), 43–51.
3 A. Rabis, P. Rodriguez and T. J. Schmidt, *ACS Catal.*, 2012, **2**(5), 864–890.
4 M. Shao, Q. Chang, J. P. Dodelet and R. Chenitz, *Chem. Rev.*, 2016, **116**(6), 3594–3657.
5 L. Huang, S. Zaman, X. Tian, Z. Wang, W. Fang and B. Y. Xia, *Acc. Chem. Res.*, 2021, **54**(2), 311–322.
6 C. Cui, X. Hu and L. Wen, *J. Semicond.*, 2020, **41**(9), 091705.
7 H. A. Gasteiger, S. S. Kocha, B. Sompalli and F. T. Wagner, *Appl. Catal., B*, 2005, **56**(1–2), 9–35.
8 X. Huang, Z. Zhao, L. Cao, Y. Chen, E. Zhu, Z. Lin, M. Li, A. Yan, A. Zettl and Y. M. Wang, *Science*, 2015, **348**(6240), 1230–1234.
9 Y. Kang, X. Ye, J. Chen, Y. Cai, R. E. Diaz, R. R. Adzic, E. A. Stach and C. B. Murray, *J. Am. Chem. Soc.*, 2013, **135**(1), 42–45.
10 D. Deng, K. S. Novoselov, Q. Fu, N. Zheng, Z. Tian and X. Bao, *Nat. Nanotechnol.*, 2016, **11**(3), 218–230.
11 X. Chia and M. Pumera, *Nat. Catal.*, 2018, **1**(12), 909–921.
12 K. Lasek, J. Li, S. Kolekar, P. M. Coelho, L. Guo, M. Zhang, Z. Wang and M. Batzill, *Surf. Sci. Rep.*, 2021, **76**(2), 100523.
13 Z. Pei, J. Gu, Y. Wang, Z. Tang, Z. Liu, Y. Huang, Y. Huang, J. Zhao, Z. Chen and C. Zhi, *ACS Nano*, 2017, **11**(6), 6004–6014.
14 H. Zhang, Y. Tian, J. Zhao, Q. Cai and Z. Chen, *Electrochim. Acta*, 2017, **225**, 543–550.
15 Y. Wang, Y. J. Tang and K. Zhou, *J. Am. Chem. Soc.*, 2019, **141**(36), 14115–14119.
16 G. Wu, K. L. More, C. M. Johnston and P. Zelenay, *Science*, 2011, **332**(6028), 443–447.
17 S. Lin, H. Xu, Y. Wang, X. C. Zeng and Z. Chen, *J. Mater. Chem. A*, 2020, **8**(11), 5663–5670.
18 C. Deng, Y. Su, F. Li, W. Shen, Z. Chen and Q. Tang, *J. Mater. Chem. A*, 2020, **8**(46), 24563–24571.
19 H. Jiang, J. Gu, X. Zheng, M. Liu, X. Qiu, L. Wang, W. Li, Z. Chen, X. Ji and J. Li, *Energy Environ. Sci.*, 2019, **12**(1), 322–333.
20 N. Karmodak, L. Bursi and O. Andreussi, *J. Phys. Chem. Lett.*, 2022, **13**(1), 58–65.
21 N. F. Rosli, C. C. Mayorga-Martinez, N. M. Latiff, N. Rohaizad, Z. Sofer, A. C. Fisher and M. Pumera, *ACS Sustainable Chem. Eng.*, 2018, **6**(6), 7432–7441.
22 Y. Wang, Y. Li and T. Heine, *J. Am. Chem. Soc.*, 2018, **140**(40), 12732–12735.
23 Y. Wang and K. Zhou, *Green Energy Environ.*, 2022, **7**(3), 525–532.
24 S. Zhao, K. Wang, X. Zou, L. Gan, H. Du, C. Xu, F. Kang, W. Duan and J. Li, *Nano Res.*, 2019, **12**(4), 925–930.
25 N. Zhang, F. Zheng, B. Huang, Y. Ji, Q. Shao, Y. Li, X. Xiao and X. Huang, *Adv. Mater.*, 2020, **32**(22), e1906477.
26 L. H. Li, J. H. Yuan, K. H. Xue, M. Xu, M. Xu, J. F. Wang and X. S. Miao, *J. Phys. Chem. C*, 2020, **124**(6), 3671–3680.
27 L. Zhao, G. Yu, X. Huang and W. Chen, *Inorg. Chem.*, 2022, **61**(4), 2284–2291.
28 T. Liu, Y. Wang and Y. Li, *J. Phys. Chem. C*, 2021, **125**(35), 19164–19170.
29 A. Mar, S. Jobic and J. A. Ibers, *J. Am. Chem. Soc.*, 1992, **114**(23), 8963–8971.
30 A. Mar and J. A. Ibers, *J. Solid State Chem.*, 1992, **97**(2), 366–376.
31 B. E. Brown, *Acta Crystallogr.*, 1996, **20**(2), 264–267.
32 E. W. Liimatta and J. A. Ibers, *J. Solid State Chem.*, 1988, **77**(1), 141–147.
33 E. W. Liimatta and J. A. Ibers, *J. Solid State Chem.*, 1989, **78**(1), 7–16.
34 W. Tremel, *Angew. Chem., Int. Ed.*, 1992, **31**(2), 217–220.
35 J. Neuhausen, V. K. Evstaf'iev, T. Block, E. W. Finckh, W. Tremel, L. Augustin, H. Fuchs, D. Voss and P. Krüger, *Chem. Mater.*, 1998, **10**(12), 3870–3878.
36 J. Neu, K. Wei, X. He, O. Delaire, R. Baumbach, Z. Feng, Y. Fu, Y. Zhang, D. J. Singh and T. Siegrist, *Phys. Rev. B*, 2019, **100**(14), 144102.
37 Y. Liu, C. Q. Xu, W. H. Jiao, P. G. Cai, B. Li, W. Zhou, B. Qian, X. F. Jiang, R. Sankar and X. L. Ke, *Tungsten*, 2021, 1–7.
38 T. Bjorkman, A. Gulans, A. V. Krasheninnikov and R. M. Nieminen, *Phys. Rev. Lett.*, 2012, **108**(23), 235502.
39 N. Mounet, M. Gibertini, P. Schwaller, D. Campi, A. Merkys, A. Marrazzo, T. Sohier, I. E. Castelli, A. Cepellotti, G. Pizzi and N. Marzari, *Nat. Nanotechnol.*, 2018, **13**(3), 246–252.
40 S. Haastrup, M. Strange, M. Pandey, T. Deilmann, P. S. Schmidt, N. F. Hinsche, M. N. Gjerding, D. Torelli, P. M. Larsen and A. C. Riis-Jensen, *2D Materials*, 2018, **5**(4), 042002.
41 M. Jin, P. Yu, C. Fan, Q. Li, P. Kong, Z. Shen, X. Qin, Z. Chi, C. Jin, G. Liu, G. Zhong, G. Xu, Z. Liu and J. Zhu, *Adv. Sci.*, 2021, **8**(24), e2103250.
42 V. Tripković, E. Skúlason, S. Siahrostami, J. K. Nørskov and J. Rossmeisl, *Electrochim. Acta*, 2010, **55**(27), 7975–7981.
43 H. A. Hansen, V. Viswanathan and J. K. Nørskov, *J. Phys. Chem. C*, 2014, **118**(13), 6706–6718.
44 F. Lu, W. Xie, D. Yi, Y. Wang, F. Zhang, Y. Xu, B. Zhou, S. Liu, X. Wang and J. Yao, *CCS Chem.*, 2021, **3**(11), 180–188.
45 Y. Zhou, Q. Gu, K. Yin, Y. Li, L. Tao, H. Tan, Y. Yang and S. Guo, *Angew. Chem., Int. Ed.*, 2022, e202201416.

46 A. Föhlisch, M. Nyberg, P. Bennich, L. Triguero, J. Hasselström, O. Karis, L. G. M. Pettersson and A. Nilsson, *J. Chem. Phys.*, 2000, **112**(4), 1946–1958.
47 A. Föhlisch, M. Nyberg, J. Hasselström, O. Karis, L. G. M. Pettersson and A. Nilsson, *Phys. Rev. Lett.*, 2000, **85**(15), 3309.
48 J. Suntivich, H. A. Gasteiger, N. Yabuuchi, H. Nakanishi, J. B. Goodenough and Y. Shao-Horn, *Nat. Chem.*, 2011, **3**(7), 546–550.
49 J. K. Norskov, T. Bligaard, J. Rossmeisl and C. H. Christensen, *Nat. Chem.*, 2009, **1**(1), 37–46.
50 C. Ling, X. Niu, Q. Li, A. Du and J. Wang, *J. Am. Chem. Soc.*, 2018, **140**(43), 14161–14168.
51 H. B. Tao, L. Fang, J. Chen, H. B. Yang, J. Gao, J. Miao, S. Chen and B. Liu, *J. Am. Chem. Soc.*, 2016, **138**(31), 9978–9985.
52 S. Zhou, X. Yang, X. Xu, S. X. Dou, Y. Du and J. Zhao, *J. Am. Chem. Soc.*, 2020, **142**(1), 308–317.
53 Y. Jiao, Y. Zheng, M. Jaroniec and S. Z. Qiao, *J. Am. Chem. Soc.*, 2014, **136**(11), 4394–4403.
54 J. K. Nørskov, T. Bligaard, J. Rossmeisl and C. H. Christensen, *Nat. Chem.*, 2009, **1**(1), 37–46.
55 I. C. Man, H. Y. Su, F. Calle-Vallejo, H. A. Hansen, J. I. Martínez, N. G. Inoglu, J. Kitchin, T. F. Jaramillo, J. K. Nørskov and J. Rossmeisl, *ChemCatChem*, 2011, **3**(7), 1159–1165.
56 M. M. Montemore and J. W. Medlin, *Catal. Sci. Technol.*, 2014, **4**(11), 3748–3761.
57 M. Andersen, S. V. Levchenko, M. Scheffler and K. Reuter, *ACS Catal.*, 2019, **9**(4), 2752–2759.
58 E. M. Fernandez, P. G. Moses, A. Toftelund, H. A. Hansen, J. I. Martinez, F. Abild-Pedersen, J. Kleis, B. Hinnemann, J. Rossmeisl, T. Bligaard and J. K. Norskov, *Angew. Chem., Int. Ed.*, 2008, **47**(25), 4683–4686.
59 A. Vojvodic, A. Hellman, C. Ruberto and B. I. Lundqvist, *Phys. Rev. Lett.*, 2009, **103**(14), 146103.
60 F. Abild-Pedersen, J. Greeley, F. Studt, J. Rossmeisl, T. R. Munter, P. G. Moses, E. Skulason, T. Bligaard and J. K. Norskov, *Phys. Rev. Lett.*, 2007, **99**(1), 016105.
61 A. Kulkarni, S. Siahrostami, A. Patel and J. K. Norskov, *Chem. Rev.*, 2018, **118**(5), 2302–2312.
62 A. Mahata, A. S. Nair and B. Pathak, *Cataly. Sci. Technol.*, 2019, **9**(18), 4835–4863.
63 Y. L. Lee, M. J. Gadre, Y. Shao-Horn and D. Morgan, *Phys. Chem. Chem. Phys.*, 2015, **17**(33), 21643–21663.
64 V. Viswanathan, H. A. Hansen, J. Rossmeisl and J. K. Norskov, *J. Phys. Chem. Lett.*, 2012, **3**(20), 2948–2951.
65 J. R. Kitchin, J. K. Norskov, M. A. Barteau and J. G. Chen, *J. Chem. Phys.*, 2004, **120**(21), 10240–10246.
66 V. Pallassana, M. Neurock, L. B. Hansen, B. Hammer and J. K. Nørskov, *Phys. Rev. B: Condens. Matter Mater. Phys.*, 1999, **60**(8), 6146.
67 F. H. B. Lima, J. Zhang, M. H. Shao, K. Sasaki, M. B. Vukmirovic, a. E. A. Ticianelli and R. R. Adzic, *J. Phys. Chem. C*, 2007, **111**(1), 404–410.
68 N. Liu, S. Zhou and J. Zhao, *Mater. Today Phys.*, 2021, **16**, 100312.
69 Y.-L. Lee, J. Kleis, J. Rossmeisl, Y. Shao-Horn and D. Morgan, *Energy Environ. Sci.*, 2011, **4**(10), 3966–3970.
70 B. Wang and F. Zhang, *Angew. Chem., Int. Ed.*, 2022, **61**(4), e202111026.
71 X. Zhu, X. Tan, K. H. Wu, S. C. Haw, C. W. Pao, B. J. Su, J. Jiang, S. C. Smith, J. M. Chen, R. Amal and X. Lu, *Angew. Chem., Int. Ed.*, 2021, **60**(40), 21911–21917.
72 Y. Chang, Y. Cheng, Y. Feng, K. Li, H. Jian and H. Zhang, *ACS Appl. Mater. Interfaces*, 2019, **11**(13), 12224–12231.
73 S. Zhou, W. Pei, Y. Zhao, X. Yang, N. Liu and J. Zhao, *npj Comput. Mater.*, 2021, **7**(1), 1–34.
74 C. F. Dickens, J. H. Montoya, A. R. Kulkarni, M. Bajdich and J. K. Nørskov, *Surf. Sci.*, 2019, **681**, 122–129.
75 S. Zhou, X. Yang, W. Pei, N. Liu and J. Zhao, *Nanoscale*, 2018, **10**(23), 10876–10883.
76 A. Tamai, Q. S. Wu, I. Cucchi, F. Y. Bruno, S. Riccò, T. K. Kim, M. Hoesch, C. Barreteau, E. Giannini, C. Besnard, A. A. Soluyanov and F. Baumberger, *Phys. Rev. X*, 2016, **6**(3), 031021.
77 W. Tremel, *Angew. Chem.*, 1991, **103**(7), 900–903.
78 A. Mar and J. A. Ibers, *J. Chem. Soc. Dalton Trans.*, 1991, **4**, 639.
79 J. Liu, H. Wang, C. Fang, L. Fu and X. Qian, *Nano Lett.*, 2017, **17**(1), 467–475.
80 A. Sufyan, G. Macam, C. Hsu, Z. Huang, S. Huang, H. Lin and F. Chuang, *Chinese J. Phys.*, 2021, **73**, 95.
81 Y. Wang and J. P. Perdew, *Phys. Rev. B: Condens. Matter Mater. Phys.*, 1991, **43**(11), 8911–8916.
82 G. Kresse and J. Furthmüller, *Phys. Rev. B: Condens. Matter Mater. Phys.*, 1996, **54**(16), 11169.
83 J. P. Perdew and Y. Wang, *Phys. Rev. B: Condens. Matter Mater. Phys.*, 1992, **45**(23), 13244–13249.
84 H. J. Monkhorst and J. D. Pack, *Phys. Rev. B: Solid State*, 1976, **13**(12), 5188–5192.
85 S. Grimme, S. Ehrlich and L. Goerigk, *J. Comput. Chem.*, 2011, **32**(7), 1456–1465.
86 A. Togo, F. Oba and I. Tanaka, *Phys. Rev. B: Condens. Matter Mater. Phys.*, 2008, **78**(13), 134106.
87 W. Tang, E. Sanville and G. Henkelman, *J. Phys.: Condens. Matter*, 2009, **21**(8), 084204.
88 R. Dronskowski and P. E. Bloechl, *J. Phys. Chem.*, 1993, **97**(33), 8617–8624.
89 V. L. Deringer, A. L. Tchougreeff and R. Dronskowski, *J. Phys. Chem. A*, 2011, **115**(21), 5461–5466.
90 S. Maintz, V. L. Deringer, A. L. Tchougreeff and R. Dronskowski, *J. Comput. Chem.*, 2016, **37**(11), 1030–1035.
91 G. Henkelman, B. P. Uberuaga and H. Jónsson, *J. Chem. Phys.*, 2000, **113**(22), 9901–9904.
92 J. K. Nørskov, J. Rossmeisl, A. Logadottir, L. Lindqvist, J. R. Kitchin, T. Bligaard and H. Jónsson, *J. Phys. Chem. B*, 2004, **108**(46), 17886–17892.